Chemical Engineering Journal 454 (2023) 140168

Contents lists available at ScienceDirect

Chemical Engineering Journal

journal homepage: www.elsevier.com/locate/cej

An *in situ* approach to entrap ultra-small iron oxide nanoparticles inside hydrophilic electrospun nanofibers with high arsenic adsorption

Nicolás Torasso [a,b], Alicia Vergara-Rubio [a,b], Reinaldo Pereira [c], Javier Martinez-Sabando [d], José Roberto Vega Baudrit [c,f], Silvina Cerveny [d,e,*], Silvia Goyanes [a,b,*]

[a] Universidad de Buenos Aires. Facultad de Ciencias Exactas y Naturales, Departamento de Física (C1428EGA), Buenos Aires, Argentina
[b] CONICET - Universidad de Buenos Aires, Instituto de Física de Buenos Aires - CONICET (IFIBA), (C1428EGA) Buenos Aires, Argentina
[c] National Laboratory of Nanotechnology, National Center of High Technology (LANOTEC-CeNAT-CONARE), 1174-1200 Pavas, San José, Costa Rica
[d] Centro de Física de Materiales (CSIC, UPV/EHU)-Materials Physics Center (MPC), Paseo Manuel de Lardizabal 5, San Sebastián 20018, Spain
[e] Donostia International Physics Center (DIPC), San Sebastián 20018, Spain
[f] Laboratory of Polymers (POLIUNA), National University of Costa Rica (UNA), Heredia, 86-3000, Costa Rica

ARTICLE INFO

Keywords:
Arsenic
Chromium
Electrospinning
Iron oxide nanoparticles
Nanofibers
Poly(vinyl alcohol)

ABSTRACT

The problem of arsenic contamination in water demands sustainable, scalable, and easy-to-implement solutions. Various nano-adsorbents flourished in the last decade, but their use alone requires additional filtering processes to avoid environmental contamination. This work presents a simple, efficient, green approach to overcome this inconvenience while maximizing adsorption capacity. We show for the first time a novel approach to synthesizing ultra-small nanoparticles (IONPs) within electrospun hydrophilic poly(vinyl alcohol) (PVA) nanofibers, avoiding NPs release into the environment when submerged in water. The in-situ synthesis favor enhanced arsenic adsorption capacity due to the excellent dispersion, tiny size, and surface availability of IONPs, reaching 3.5 mg/g at 10 μg/L. We show that IONPs alter the polymeric matrix properties, such as the glass transition temperature and crystallinity, by preventing the formation of strong hydrogen bond inter/intramolecular interactions of PVA. Insolubility and swelling capacity are essential characteristics of this membrane, which allow solution interchange for arsenic adsorption onto IONPs. Isotherm studies show that the increase from 1 wt% to 3 wt% of IONPs content decreases the active sites for adsorption per mass of IONPs. Still, it does not alter the reusability of the membrane, which reaches at least 3 adsorption cycles with 80 % efficiency. We discuss the adsorption mechanisms and show that phosphate anions partially inhibit As(V) adsorption and that the membranes are also highly capable of removing Cr(VI), independently of the presence of Ni(II).

1. Introduction

Water is a critical liquid on our planet since our biology, chemistry, and other physiological characteristics are based on it. Furthermore, water is a human right and is included as one of the global 17 sustainable development goals (SDGs) for 2030 [1]. However, today, one in three humans worldwide does not have access to safe drinking water. Millions of people in developing and developed countries [2,3] are affected by drinking water contaminants, particularly emerging contaminants [4] such as heavy metals or pharmaceuticals [5]. Among them, arsenic is considered one of the most dangerous hazards in drinking water[6], and at least 230 million people in 108 countries have been drinking water containing arsenic at levels above the WHO provisional guideline value of 10 μg/L [7].

Numerous water purification technologies have been proposed, mainly based on membrane filtration, distillation, reverse osmosis, adsorption, and ion exchange [8]. Nevertheless, most require several stages, increased investment and operating costs, high-energy requirements, and reliance on materials with a high environmental footprint [9]. Among them, adsorption accompanied by nanotechnology is especially favorable because it involves materials extracted from by-products, and it meets a high removal efficiency with sustainability.

* Corresponding authors at: Centro de Física de Materiales (CSIC, UPV/EHU)-Materials Physics Center (MPC), Paseo Manuel de Lardizabal 5, San Sebastián 20018, Spain (S. Cerveny). Universidad de Buenos Aires. Facultad de Ciencias Exactas y Naturales, Departamento de Física (C1428EGA), Buenos Aires, Argentina (S. Goyanes).
E-mail addresses: silvina.cerveny@ehu.es (S. Cerveny), goyanes@df.uba.ar (S. Goyanes).

https://doi.org/10.1016/j.cej.2022.140168
Received 14 July 2022; Received in revised form 25 October 2022; Accepted 30 October 2022
Available online 4 November 2022

However, the drawbacks of the use of bulk nano-adsorbents (such as nanoparticles) include their tendency to agglomerate (with the consequence of decreasing efficiency [10]) and the additional contamination produced if they are directly used in the water system [11]. On the other hand, the major problem with using NPs is their toxicity to humans and environmental impact [12]. Even biodegradable nanoparticles may accumulate within cells and lead to gene alternations [13]. Consequently, retaining the NPs to be used safely is a central problem in nanotechnological applications.

In this context, nanoparticle confinement (and immobilization) occupies a central role in developing materials for water remediation, and it is a certain and promising alternative to using bulk adsorbents for water remediation [14]. Specifically, for arsenic removal, studies of the last decade show that iron oxide nanoparticles are excellent arsenic adsorbents [15] due to their enhanced surface-to-volume ratio, high affinity towards arsenic, low energy consumption, reversibility, and high selectivity [10]. A particular way to immobilize iron oxide nanoparticles is via electrospinning, a versatile and scalable membrane fabrication technique, which allows the production of nano- and submicron polymeric fibers for a wide range of applications, including water treatment, oil water filtration, particle filtration, and microorganisms filtration [16–20]. Generally, preparing nano-adsorbent filled with nanoparticles involved two steps: the synthesis of NPs and their dispersion in the polymeric matrix. However, this procedure raises other issues, such as the significant size of the NPs, the limitation of their quantity included in the polymer, and their dispersion within the polymer. To overcome all these issues at a time, we explored the in-situ synthesis of the NPs during the electrospinning process.

A suitable polymer to prepare membranes using electrospinning is poly(vinyl alcohol) (PVA). To start, PVA is biodegradable [21], making it perfect green for water purification Secondly, it can dissolve in several solvents (a necessary feature for electrospinning), and particularly in water. Thirdly, and more importantly, PVA can crosslink or dehydrate to become insoluble without losing its swelling capacity [22]. This is an essential character as the success of the remediation procedures depends entirely on the swelling of the membranes. The membranes must swell during the remediation process, allowing contaminants to reach the NPs. Therefore, PVA is more appropriate than other polymers to develop water treatment membranes. Previous studies of our group have successfully confined iron oxide nanoparticles in electrospun PVA nanofibers using a two-step procedure. The first step was the synthesis of NPs, and the second was their suspension in a PVA solution by ultrasonication before electrospinning. This method showed that NPs were excellently dispersed inside the nanofibers but, unfavorably, with a minor amount of NPs (0.14 wt%) [23].

With the main goal of confining a higher amount of NPs in the membrane, we explored the *in situ* synthesis of the NPs during the electrospinning process. This method is more straightforward as it is a one-step procedure. Additionally, it provides further advantages like better NPs growth control, steric stabilization, and homogeneous distribution of salt precursors. In this sense, there was a previous attempt in the literature. Wang *et al.* [24] reported electrospun PVA nanofibers containing *in situ* synthesized magnetic iron oxide NPs. Still, these fibers were not treated to yield a water-insoluble material, and, in turn, they did not assess contaminant adsorption. In addition, the electrospun solution was dialyzed, which is expensive, time-consuming, and it can potentially contaminate the sample.

This work shows a novel approach to synthesizing *in situ* ultra-small iron oxide NPs in electrospinning solutions. We obtained self-standing membranes with a considerable quantity of NPs compared with other membranes in the literature. Moreover, these membranes have high arsenic adsorption capacity and can reduce arsenic concentration below 10 μg/L. We assess the effect of increasing NPs content in nanofibers morphology and arsenic adsorption performance. We show the NPs distribution inside the nanofibers using TEM microscopy and their interaction with the polymeric matrix via DSC and TGA. Moreover, increasing NPs content produces agglomeration, consequently reducing arsenic adsorption efficiency. Since disposing of the membranes after use may have an adverse environmental impact, we also analyze their desorption and reuse. Here, we probed three reuse cycles with high removal effectiveness (84 %) and without migration of iron to the water. Finally, we show that the methodology to make these membranes can also be used for the adsorption of heavy metals such as Cr(VI) and Ni(II), with a remarkable adsorption capacity for Cr(VI) which, in addition, is independent of the Ni content.

2. Materials and methods

2.1. Materials

PVA (Mowiol 10–98) with $M_W = 61{,}000$ g/mol and 98 % hydrolysis was purchased from Sigma Aldrich (Argentina). For the SPIONs *in situ* synthesis, reagent grade NaOH (Sigma), $FeCl_3$ (Sigma), and $FeSO_4 \cdot 7H_2O$ (Biopack-Argentina) were used with no further purification. Deionized distilled water with a resistivity of 18.2 MΩ.cm and purged with argon gas for 30 min was used to prepare electrospinning solutions. For arsenic (V) dilutions, we used a 1000 mg/L As(V) standard solution for ICP (Sigma Aldrich) and DI water. Acetate buffers were prepared using acetic acid (Sigma Aldrich 99.8 %) and sodium acetate trihydrate (Sigma reagent plus $> = 99$ %). MES buffers were prepared using MES sodium salt (Sigma, ≥99 %) and MES monohydrate (Sigma, BioXtra ≥99.0 %). Phosphate solution was prepared from sodium phosphate monobasic (H_2NaPO_4, Fluka ≥99.0 %). Chromium (VI) and nickel (II) solutions were prepared using chromium (VI) oxide (Aldrich) and nickel (II) chloride (98 %, Aldrich).

2.2. Membrane fabrication

First, 3 g of PVA were dissolved in 19 mL of water by constant stirring at 85 °C. Next, $FeSO_4 \cdot 7H_2O$ and $FeCl_3$ were separately dissolved in 1 mL of water. After cooling of PVA solution to room temperature, iron solutions were added and stirred until a homogeneous mixture was obtained. Finally, a fixed amount of 2 M NaOH solution was added dropwise at 4.0 mL/h under ultrasonic batch sonication (40 kHz, 80 W) and mechanical stirring to force the precipitation of iron oxide nanoparticles in the presence of PVA (see solution preparation images in Fig. S1). The amount of salt was varied depending on the NPs fraction and according to the following precipitation reaction:

$$2\ Fe^{3+} + Fe^{2+} + 8\ OH^- \rightarrow Fe_3O_4 + 4\ H_2O$$

NaOH was added in 5 % excess. Then, the solutions were electrospun to give PVA-1, PVA-2, and PVA-3 membranes containing 1 %, 2 %, and 3 % of iron oxide NPs with respect to PVA. All electrospinning solutions are stable for at least one week and no precipitate is observed in that time. A 12 % PVA solution without NPs was used to electrospin a control membrane (PVA-0). A summary of solution properties is shown in Table 1. Electrospinning was performed at 30 kV, using a custom 6-needle injector at 11 cm from the grounded collector. Total flow rate was 2.5 mL/h for PVA-1 and 1.8 mL/h for PVA-2 and PVA-3. Relative humidity and temperature were kept in the range 50–60 % and 24–26 °C, respectively. Before use, all electrospun membranes were heat-treated in an oven at 190 °C for 15 min to give water stability and then washed in

Table 1
Physical and chemical properties of the electrospinning solutions measured at (26 ± 1) °C.

Solution	Viscosity [cP]	Conductivity [mS/cm]	pH
PVA-0	242	0.69 ± 0.02	5.50 ± 0.03
PVA-1	216	3.44 ± 0.02	5.54 ± 0.03
PVA-2	220	6.10 ± 0.02	6.40 ± 0.03
PVA-3	231	8.78 ± 0.02	6.06 ± 0.03

deionized water (30 g/L) for 3 h at 120 rpm orbital shaking and until constant pH was reached to remove reaction by-products. A schematic illustration of the process is shown in Fig. 1(a). The membrane weight was compared before and after a second identical washing cycle using an analytical balance with the main goal of monitoring possible weight loss (Denver Instruments APX-200). This procedure was repeated after six months of water submersion.

2.3. Characterizations

Microscopy. The membrane morphology was revealed using a Scanning Electron Microscopy (FEI Helios 450S) equipped with EDX. Images were obtained using electron high tension (EHT) 2 kV, 100,000 × magnification, and a working distance of 3.6 mm in carbon-coated samples. High-resolution transmission electron microscopy (HR-TEM) was performed with a JEOL JEM 2011 operating at 120 kV. Samples were prepared by electrospinning over Cu grids.

TGA. Thermogravimetric analysis was performed with a TA Instruments Q500 at a rate of 5 K/min under a nitrogen atmosphere on 25 mg samples. Gas was changed to air at 500 °C to complete combustion and analyze the solid residue. Weigt loss values were normalized to the mass of the membranes after water evaporation, near 130 °C. The NPs load was quantitatively determined as the solid residue of the membrane after subtracting the solid residue of a control membrane without NPs.

XRD. X-ray powder diffraction patterns of the samples were collected by using a Philips X'pert PRO automatic diffractometer operating at 40 kV and 40 mA, in theta-theta configuration, secondary monochromator with Cu-Kα radiation (λ = 1.5418 Å) and a PIXcel solid state detector (active length in 2θ 3.347°). Data were collected from 5 to 80° 2θ, step size 0.026° and time per step of 1200 s at RT (total time 4 h, scan speed 5.6°/ms). A fixed soller and divergence slits giving a constant volume of sample illumination were used. Iron oxide databases were obtained from JCPDS (magnetite 01–088-0315), American Mineralogist Crystal Structure Database (akaganeite 1349 and lepidocrocite 0020688) and Materials Project (hematite mp-19770 and goethite mp-605437) [25,26].

FTIR. Spectra were recorded from 4000 cm^{-1} to 600 cm^{-1} with a resolution of 4 cm^{-1} in ATR mode using a Jasco FTIR-4100 (Japan).

DSC. DSC studies were carried out using a TA Q2000 LNCS at 5 K/min, using non-hermetic aluminum capsules, and running a previous drying sequence up to 130 °C to suppress the plasticizer effect of water in the samples. Glass transition of the materials (T_g) was obtained using the bisector method.

Porosimetry. Nitrogen adsorption/desorption measurements were performed with an Autosorb iQ3 instrument (Quantachrome Instruments) in the relative pressure range P/P0 from 7×10^{-6} to 1. Before the adsorption analysis, the samples were outgassed for 24 h at 100 °C. The experiments were accomplished with a large sample (approximately 1 g).

NPs retention. The possible leaching of iron oxide nanoparticles was evaluated by determining the total iron in water after a simulated adsorption process (dose of 30 mg_{IONPs}/L in 10 mL of deionized water) and for PVA-1 and PVA-2 membranes. After 24 h, the membranes were removed and the solution was digested with 500 µL of HNO_3 (63 wt%, Biopack-Argentina). The iron concentration was determined by Flame Atomic Absorption Spectroscopy (FAAS) using air/acetylene (Shimadzu AA 6800 with a Shimadzu hollow cathode lamp source).

2.4. Adsorption experiments

All arsenic adsorption experiments were performed in batch, in 10 mL solutions using a dose of 30 mg/L of IONPs (i.e., 30 mg of membrane for PVA-1, 15 mg for PVA-2, and 10 mg for PVA-3) under orbital shaking at 120 rpm and at (25 ± 1) °C. The pH of solutions was kept constant using either a 25 mM acetate buffer for pH 4 and 5 or a 4 mM MES buffer for pH 6.5 and 7.5. Adsorption isotherms were measured at varying initial concentrations of As(V) ranging from 100 µg/L to 2,000 µg/L, prepared from a 10 mg/L stock solution. Equilibrium arsenic concentration (C_{eq}) was measured using an inductively-coupled-plasma atomic emission spectrophotometer (ICP-AES) Horiba Jobin Yvon Activa. Aliquots were taken at 48 h to measure C_{eq}, and adsorption capacity (q) was calculated as:

$$q = \frac{C_0 - C_{eq}}{d} \tag{1}$$

where C_0 is the initial arsenic concentration and d is the adsorbent dose.

The adsorption isotherms were fitted using both Langmuir and Freundlich models (Eqs. (2) and (3), respectively), given that they are usually employed to describe arsenic adsorption onto iron oxides [11]:

$$q(C_{eq}) = \frac{q_M C_{eq}}{C_{eq} + \frac{1}{K_L}} \tag{2}$$

$$q(C_{eq}) = A C_{eq}^{\frac{1}{n}} \tag{3}$$

where q is the adsorption capacity, C_{eq} is the equilibrium concentration, q_M is the maximum adsorption capacity, and K_L, A, and n are constants of the models [27].

For kinetic experiments, initial concentration was 600 µg/L and pH 5 fixed using a buffer solution. We measured arsenic concentration between 15 min and 48 h. Data were analyzed using non-linear fittings of the pseudo-second order (PSO, Eq. (4)), pseudo-first order (PFO, Eq. (5)) and Weber-Morris (WM, Eq. (6)) models [27].

$$q(t) = \frac{t}{k^{-1} q_M^{-2} + \frac{t}{q_M}} \tag{4}$$

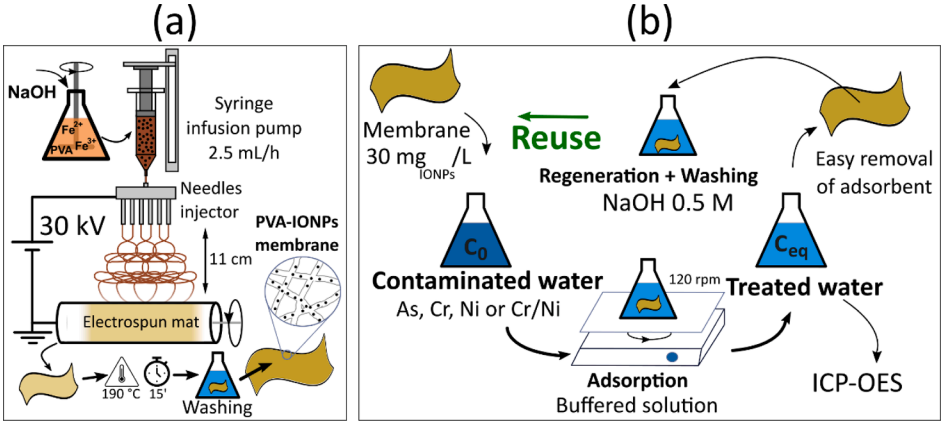

Fig. 1. Scheme of the PVA-IONPs production process. (b) Scheme of batch adsorption experiments and regeneration of the adsorbent.

$$q(t) = q_M[1 - \exp(-kt)] \quad (5)$$

$$q(t) = k\sqrt{t} \quad (6)$$

where q_M is the adsorption capacity at equilibrium and k is the characteristic time-related constant that indicates the adsorption speed at the beginning of the adsorption process. PFO and PSO equations are usually employed in the literature for modeling adsorption of arsenic onto adsorbent nanomaterials based on electrospun nanofibers [28,29] and iron oxides [30]. Weber-Morris model was also tested to assess intraparticle diffusion.

For regeneration and reusability studies, PVA-IONPs membranes were subjected to three adsorption cycles (dose of 30 mg_{IONPs}/L) followed by desorption and washing. For adsorption, a solution of 2 mg/L As(V) buffered at pH 5 was used, and the final concentration was measured at 24 h. Desorption was performed using a 0.5 M NaOH solution under orbital shaking at 120 rpm for 8 h. For washing, the membranes were rinsed three times with deionized water. A scheme of the adsorption experiments is shown in Fig. 1 (b). Cr(VI) and Ni(II) adsorption were tested using 10 mL solutions containing initial concentrations of 556 μg/L and 463 μg/L, respectively. Experiments were conducted using a PVA-2 membrane with a dose of 60 mg/L of IONPs. The pH was fixed at 5 using a buffer solution. Removal efficiency (RE) was calculated as:

$$RE = \left(1 - \frac{C_{eq}}{C_0}\right) \times 100\% \quad (7)$$

The effect of competing phosphate anion in solution was tested using 10 mL solutions containing 600 μg/L of As(V) and varying the phosphate concentration from 150 to 1500 μg/L. Experiments were conducted using a PVA-3 membrane with a dose of 30 mg/L of IONPs and at two different pH values using buffer solutions (pH 4 and pH 5).

3. Results and discussion

The electrospinning solutions were successfully electrospun under optimized conditions providing homogeneous, self-supporting membranes containing ultra-small iron oxide nanoadsorbents. Heat treatment produced water insolubility and polymer dehydration, observed as a weight loss of (7.5 ± 1) %, size shrinking, and a slight color shift to brown (see Fig. S2) [31]. The so-obtained membranes are stable in water for at least six months (see Fig. S3). According to gravimetric measurements, no weight was lost within instrumental error (0.33 wt%). Fig. S4 shows the unaltered structure of the nanofibers after that time. Fig. 2(a) shows SEM images of the membranes after being washed with water. The typical porous structure of electrospun nanofibers is observed, which is optimal for microfiltration because it allows water interchange within the nanofibers and gives low-pressure drop during water filtration. The wrinkled appearance of the nanofibers is due to submersion in water, as can be observed by comparing them with electrospun membranes after heat treatment and before submersion (Fig. S5). These changes are explained by tensions created at the boundaries between amorphous and crystalline zones due to their different response to the swelling process [23].

Average nanofibers diameter decreases with IONPs content from (129 ± 4) nm to (96 ± 4) nm, as depicted in Fig. 2(b). This is because the dissolved ions in the electrospinning solution raise conductivity and favor jet elongation in the presence of the electric field (see Table 1) [32]. In fact, the increase in conductivity limits the application of this production method for higher IONPs content. Solutions with higher NP content were electrospun but resulted in a significant loss of solution by dripping at the tip of the needles, more inhomogeneities in the membrane due to the ejection of droplets into the collector, and an increase in the number of beads in the nanofibers. Despite these limitations, finer fibers are desirable because of readily accessible IONPs inside the polymeric matrix due to increased specific surface area.

Iron content does not change appreciably after washing, as shown by EDAX analysis. Therefore, the membrane production method proposed herein can successfully entrap IONPs within the nanofibers and avoid their release to the environment when submerged in water. Moreover, it shows that washing the sample with deionized water is sufficient to remove the remaining counter-ions of the synthesis (sulfur, chloride, and sodium). Given that EDX is not suitable for an accurate quantification at the low IONPs concentration of the samples, the iron oxide content was obtained from the combustion residual in TGA (see Fig. 5 (a)). To evaluate possible leaching of IONPs, a more accurate approach is discussed at the end of this section.

Ultra-small iron oxide nanoparticles within the nanofibers of each membrane can be observed in TEM images, shown in Fig. 3. In situ synthesis in the presence of a viscous PVA solution limits the growth of the nanoparticles, as can be appreciated in their extent (less than 4 nm), especially compared to the size obtained in previous works (9 nm) without the presence of a stabilizer [23]. Increasing IONPs content also increases the number of agglomerates (see PVA-2). It provides more

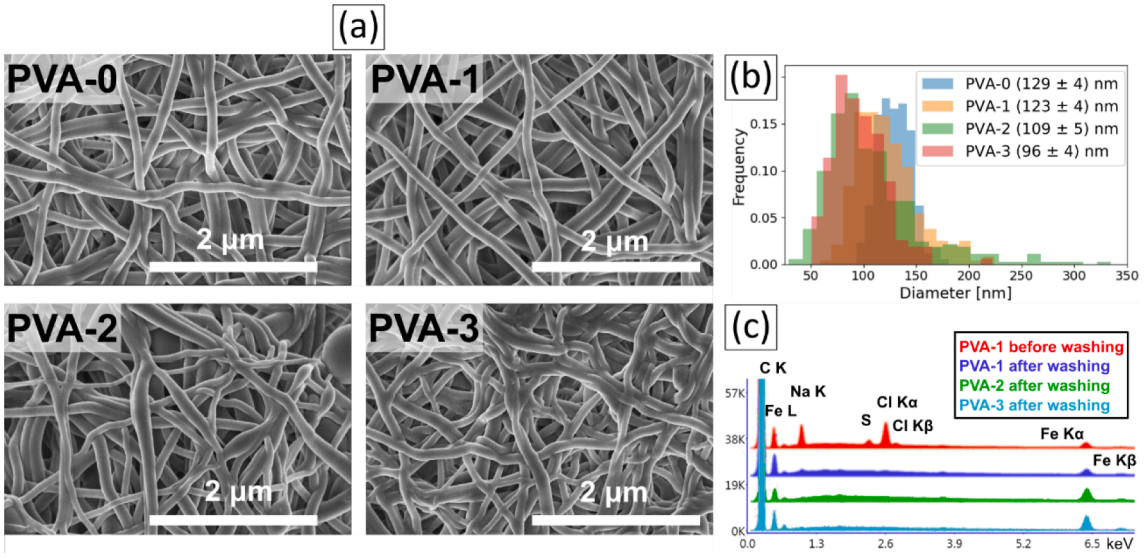

Fig. 2. (a) SEM microscopy of the electrospun membranes containing 0, 1, 2, and 3% IONPs after washing with water (b) nanofiber diameter histograms for each sample. (c) EDAX spectra of the membranes after washing. As a reference, the spectrum of PVA-1 before washing is also shown.

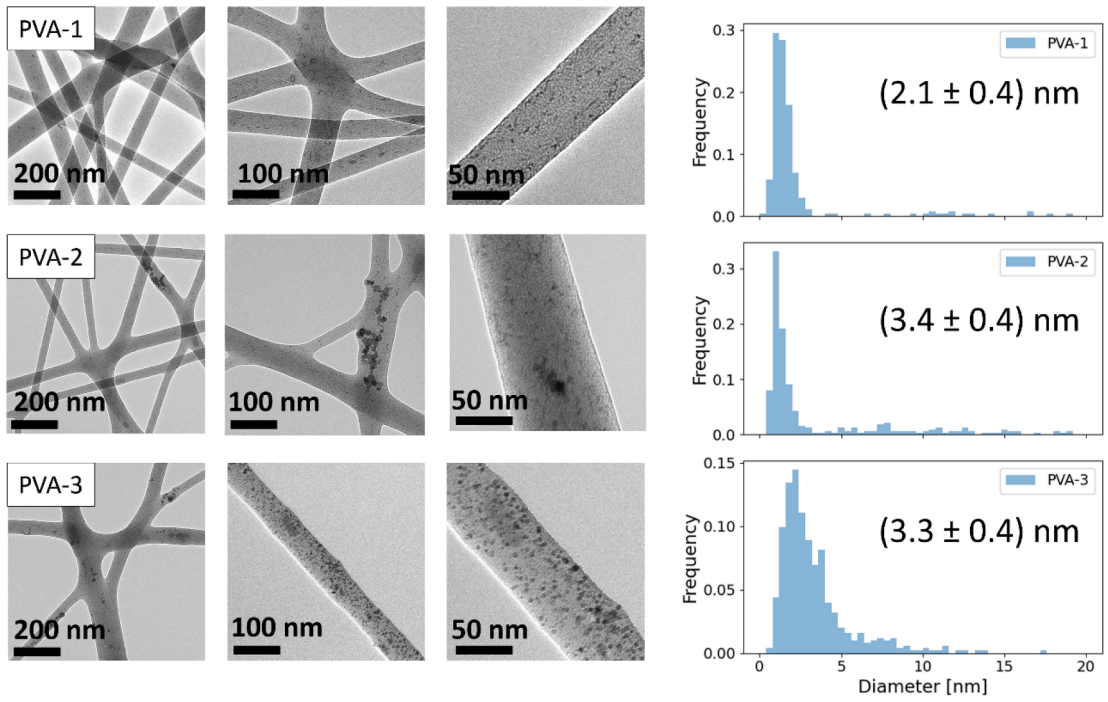

Fig. 3. TEM microscopy of the electrospun membranes containing 1, 2, and 3% IONPs (PVA-1, PVA-2, and PVA-3, respectively). Histograms of nanoparticle diameters are also shown with the corresponding mean diameter.

precursor salts per unit volume, which in turn gives bigger IONPs ((3.3 ± 0.4) nm for PVA-3 compared to (2.1 ± 0.4) nm for PVA-1) and a broader size distribution. Despite having approximately the same mode, the mean value of PVA-2 IONPs significantly increases due to the presence of agglomerates. The distribution of PVA-3 IONPs significantly broadens and becomes asymmetric, probably due to more reactants, which also increases the distribution mode. There are no significant differences between the measured mean values of PVA-2 and PVA-3, given the images resolution of 0.3 nm. Every image shows that IONPs are confined inside the nanofibers, and that the composite has a significant amount of interphase between the polymer and IONPs.

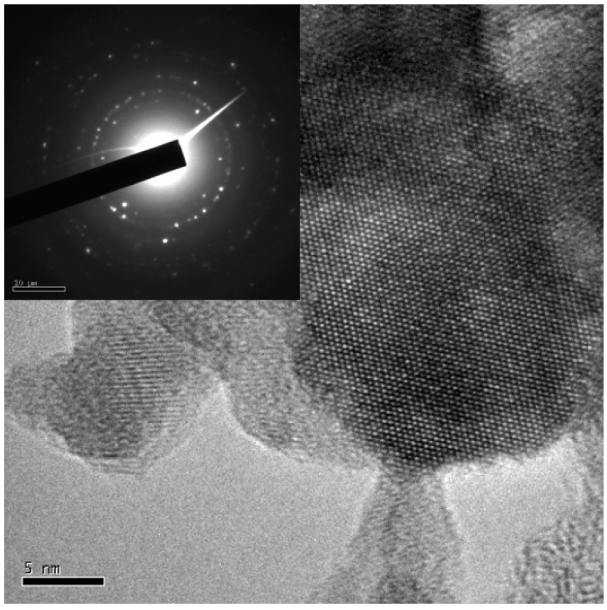

Fig. 4. HR-TEM of an agglomerate in PVA-2 membrane. Inset shows electron diffraction pattern.

Fig. 4 shows an HR-TEM image of a single agglomerate in the PVA-2 membrane. It can be seen that the crystalline nature of the IONPs agrees with DRX studies (see Fig. 6). The presence of rings in the electron diffraction pattern confirms that the structure comprises an agglomerate of individual IONPs.

Fig. 5(a) shows the thermal degradation curves of the membranes. The thermal degradation of pure PVA (PVA-0) has three distinct regions. The first one (80–150 °C) is associated with free water evaporation, the second (200–350 °C) with chain decomposition (starting with OH groups), and the third (350–450 °C) with subproducts degradation due to cyclic conjugated compounds [33]. Air-gas inlet was opened at 500 °C, which allows the quantification of the solid residue of the membranes, resulting in (1.05 ± 0.14) %, (2.0 ± 0.2) %, and (3.2 ± 0.2) % for PVA-1, PVA-2, and PVA-3 respectively. These results are consistent with the proportion used in the electrospinning solutions, proving that IONPs do not precipitate during the electrospinning process. Although heating in the presence of air could change the composition of iron oxides in the sample, the expected change in weight percent is negligible [34]. For example, the transformation of magnetite to hematite would result in a 3 % weight gain [35].

Fig. 5(a) shows that adding IONPs results in earlier degradation of the main chain. In the synthesis process, the iron oxide nanoparticles interact with the hydroxyl group of PVA, preventing intermolecular hydrogen bonding between the polymer chains [36,37]. This reduction in degradation temperature was also observed in PVA/PAA nanofibers after adding Fe_3O_4 NPs [38]. Conversely, the IONPs increase the stability of the subproducts (350–450 °C), which has already been observed in the PVA matrix filled with modified IONPs [38,39].

DSC studies show that the addition of IONPs alters both the amorphous and crystalline regions of the polymer (Fig. 5(b)). The presence of IONPs shifts the T_g to lower temperatures (from 105 °C to 86 °C), suggesting an increased free volume [40,41]. Regarding the crystalline region, PVA-0 melting involves two different processes, as indicated by the peaks at 213 °C and 218 °C. The presence of IONPs inhibits the first melting process, meaning that one of the crystalline structures cannot form in the presence of NPs. This fact also reduces the crystallinity from 47 % for PVA-0 to 36–40 % for samples containing IONPs. Finally, the

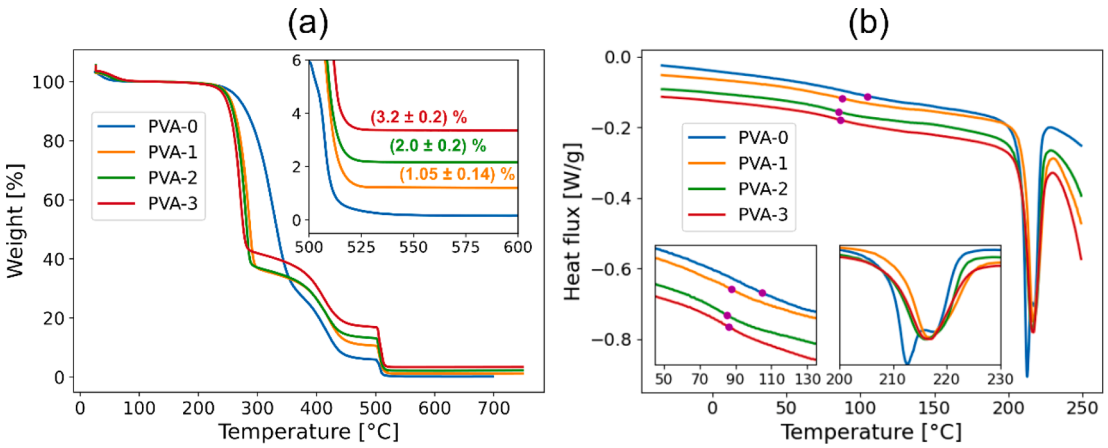

Fig. 5. (a) TG analysis of the membranes containing different amounts of IONPs. Inset shows the char residue region after opening the air-gas valve at 500 °C. (b) DSC analysis of the membranes. Curves were vertically shifted for better visualization. Insets show the regions of the polymer's glass transition (left) and melting (right). Purple dots indicate the glass transition temperature.

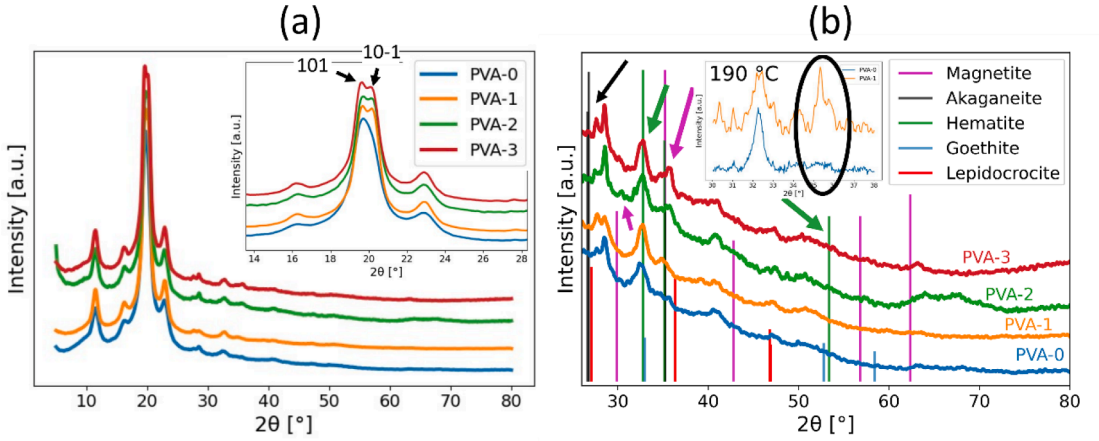

Fig. 6. (a) X-ray diffraction patterns of PVA-0, PVA-1, PVA-2, and PVA-3 membranes. Inset shows a close-up of the main crystalline peak of PVA. (b) Close-up view in the region of iron oxides main diffraction angles. Inset shows measurement at 190 °C and a distinctive peak in the PVA-1 sample compared to PVA-0.

presence of IONPs broadens and shifts the melting peak at 219 °C to a lower temperature, and more heterogeneities in the crystallites explain this behavior.

Crystallinity changes due to the presence of IONPs can also be observed in the X-ray diffraction pattern of the membranes, shown in Fig. 6. It is evident that the IONPs act as nucleation centers favoring the growth of the 10-1 diffraction plane at 20° [42], in agreement with the DSC melting studies. Fig. 6(b) shows a close-up of the region comprising the main diffraction peaks of some iron oxides and hydroxides that could form during the *in situ* synthesis, such as magnetite, maghemite, akageneite, goethite, and hematite [43]. Different from the *ex-situ* synthesis in which a single iron oxide can be easily obtained, these results suggest that the ultra-small IONPs synthesized herein show a combination of iron oxides. The most prominent diffraction peak in the region of iron

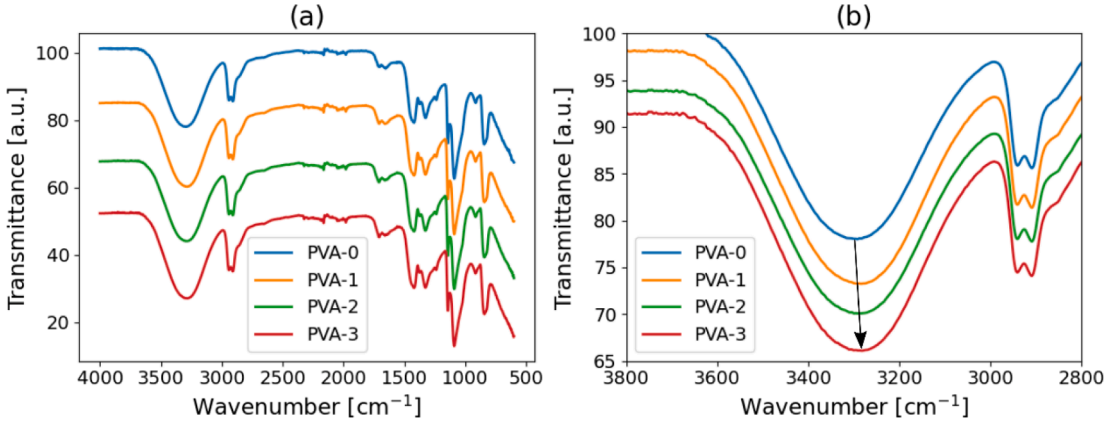

Fig. 7. (a) FTIR spectra of the membranes PVA-0, PVA-1, PVA-2, and PVA-3. (b) Close-up showing the shift in O—H vibration band.

oxides is located at 35.5° and can be assigned to either magnetite, maghemite, or akageneite. Peaks associated with these iron oxides are pointed with arrows. The appearance of this peak was further confirmed by measuring the region between 30° and 38° near the melting temperature of PVA to reduce the interference effect of PVA crystallites on the diffraction pattern (inset of Fig. 6(b)).

The FTIR spectra of the PVA-IONPs membranes after being washed are shown in Fig. 7. The samples were heat-treated, washed, and dried following the methodology described in Material and Methods. All the samples presented the characteristic bands of PVA: at 3300 and 1088 cm^{-1}, corresponding to the stretching vibration of the O—H and C—O bonds, respectively. The bands at 2939 cm^{-1} and 2909 cm^{-1} are related to asymmetric and symmetric stretching vibrations of the C—H bond in the CH_2, at 1430 cm^{-1} corresponding to bending vibrations of C—H in the CH_2 group, and at 845 cm^{-1} to stretching vibration of C—C bonds.

As shown in Fig. 7(b), the absorption band of the O—H bond is shifted to a lower wavenumber with the presence of IONPs, demonstrating the presence of hydrogen bonds. Kayal and Ramanujan stated that the surface of IONPs attach through hydrogen bonds to —OH groups in PVA [44]. This chemical interaction was also proposed by Lee *et al.* when synthesizing magnetite in the presence of PVA (up to 2 % of PVA with respect to the iron oxide)[45]. Similarly, the shift can be associated with the coordination of iron ions with the hydroxyl groups in the PVA structure [36].

Nitrogen adsorption studies (shown in Fig. S6 in SI) show that PVA nanofibers with NPs have barely larger pore sizes than nanofibers without NPs (12.3 nm for PVA-1 compared to 11.1 nm for PVA-0). Apart from these nanometric pores, both membranes are non-porous, as seen in the low total pore volume values obtained (10 cm^3/kg for PVA-0 and 5 cm^3/kg for PVA-1). These results are in accordance with IONPs entrapped between polymeric chains that prevent polymeric chains from interacting.

The earlier main chain degradation, the decrease of T_g, the shift in FTIR O—H vibration band, and the reduction of crystallinity degree indicate that the ultra-small IONPs prevent the strong hydrogen bond interaction of PVA. As already seen in the TEM images, these characteristics imply that IONPs were successfully entrapped within the nanofibers, as depicted in Fig. 8. Thus, these membranes can be used to adsorb contaminants from water. We show in the following experiments the ability to deep-treat As(V) contaminated water, starting from naturally occurring concentrations of As(V).

Arsenic adsorption onto iron oxides strongly depends on the pH of the medium [30]. Thus, adsorption isotherms were measured at fixed pH values using buffer solutions, shown in Fig. 9(a). PVA-1 membranes can remove arsenic from 120 μg/L to less than the WHO limit of 10 μg/L, with a tiny dose of 30 mg_{IONPs}/L. This performance surpasses that reported in the literature for iron oxide nanoparticles (see Table 2). It can be attributed to both the excellent dispersion of IONPs in the polymer matrix, which maximizes surface availability, and the ultra-small size of the nanoparticles (less than 5 nm, see Fig. 3), which maximizes specific surface area. The specific surface area of spherical particles is $3/(\rho\ r)$, where ρ is the material's density and r the radius of the sphere. By taking *r* as the average NP diameter for PVA-IONPs membranes, an estimation of specific surface area for each membrane yields 552 to 772 m^2/g for PVA-1, 341 to 477 m^2/g for PVA-2, and 351 to 491 m^2/g for PVA-3. Given that the exact composition of the IONPs is unknown, intervals were calculated using the higher and lower densities of the proposed crystal types obtained from XRD studies [46]. The hydrophilic nature of PVA and its underwater swelling capability is essential to allow solution interchange [22,23]. Fig. 9(a) shows that the arsenic adsorption capacity of the membranes is optimal at pH 5 and drops to at least 32 % of its value for pH $\geq$ 6.5, as can be seen in the inset of Fig. 9(a). This is expected, given that As(V) species form both inner sphere and outer spheres complexes with iron oxide particles which immobilize soluble arsenic species [15,47]. The outer sphere complexes are electrostatic in nature and result from the interaction between the surface of positively charged nano iron oxide surface and As(V) oxyanion species at a given pH [8]. Nano iron oxides have shown a pHpzc between 5.7 and 7.6 [48,49], and in this pH range the $H_2AsO_4^-$/$HAsO_4^{2-}$ species are present in the reaction medium[50]. On the other hand, the inner sphere complexes are based on Lewis acid-base interaction between As(V) oxyanions and the iron coordination sphere through ligand exchange reactions [8]. Both $H_2AsO_4^-$/$HAsO_4^{2-}$ are Lewis bases or ligands with high affinity for Lewis acid sites such as iron in oxide nanoparticles to yield mono or bidentate complexes [8,51]. At higher pH values, the surface of the IONPs loses its positive charge needed to interact with arsenate anions, and in consequence, it reduces adsorption capacity by decreasing electrostatic interaction. Also, the ligand exchange is reduced at higher pH as the OH^- groups predominate in the reaction medium. Isotherms measured at pH 4 have similar adsorption performance to pH 5 for low equilibrium concentrations, but it drops above $\approx$ 500 μg/L. At pH values lower than 5, some arsenate ions may neutralize and lose their charge, which is needed for ligand exchange to occur [15]. In consequence, pH 5 buffered solutions were used in the following experiments.

Freundlich model best fits the adsorption isotherms of PVA-IONPs membranes, even at different pH values. This indicates the presence of heterogeneous active sites and multilayer adsorption on the surface of the IONPs [11,52]. Freundlich model was reported as the best model for some works concerning iron oxyhydroxides (GFH) and iron oxide nanoparticles (IONPs) [49,53–55]. Fit results are shown in Supplementary Information (Table S1).

Fig. 9(b) shows the arsenic adsorption performance of the PVA-1, PVA-2, and PVA-3 membranes at the same IONPs dose. It becomes clear that the adsorption capacity of the IONPs depends on the electrospinning solution synthesis and the nanofiber formation conditions, which determine the IONPs size, their distribution along the nanofibers, and their tendency to agglomerate. The adsorbent capacity of iron oxides is directly related to their surface chemistry. For magnetite nanoparticles, for example, arsenate anions mainly form inner sphere complexes with iron atoms on the surface [15]. It is then expected that an increase in specific surface area would lead to better adsorption. PVA-1 has the highest adsorption capacity, likely because of the better dispersion of the IONPs in the polymeric matrix and their smaller size (see Fig. 3), which maximizes sites available for adsorption (specific surface area). PVA-2 and PVA-3 have similar adsorption isotherms,

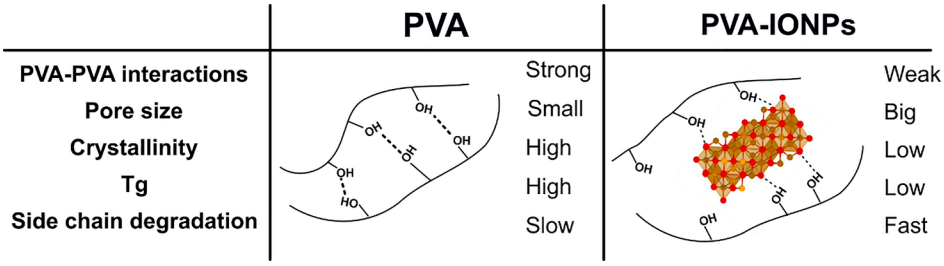

Fig. 8. Diagram showing the proposed interaction and structure of IONPs and PVA compared to the membrane without IONPs.

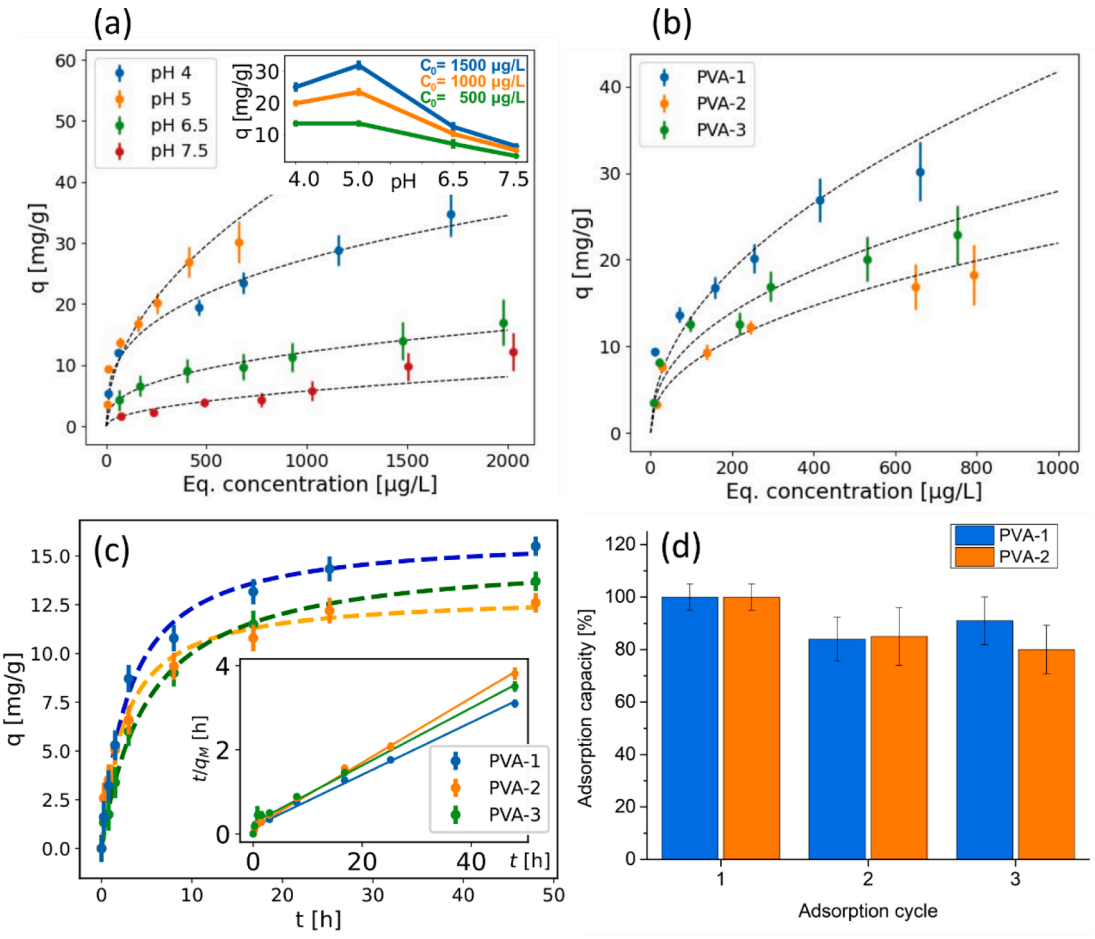

Fig. 9. (a) Adsorption isotherms at different pH values using the PVA-1 membrane. Inset shows the variation of adsorption capacity as a function of pH for selected initial concentrations. (b) Adsorption isotherms of PVA-1, PVA-2, and PVA-3 membranes at pH 5 and a dose of 30 mg_{IONPs}/L. Dashed lines show non-linear fittings using the Freundlich model. (c) Adsorption kinetics of PVA-1, PVA-2, and PVA-3 membranes. Initial arsenic concentration was 600 µg/L and pH 5 fixed using a buffer solution. Dashed lines are fittings using the PSO model. Inset shows linearized data according to the PSO model and their corresponding linear fit lines. (d) Relative As(V) adsorption capacity of PVA-1 and PVA-2 membranes on each adsorption cycle, followed by regeneration in an alkaline solution.

Table 2
Adsorption capacity of iron oxide adsorbents at 10 µg/L.

Adsorbent	Size [nm]	pH	Dose [mg/L]	Adsorption capacity at 10 µg/L [mg/g]	Reference
Ultrafine γ-Fe_2O_3	3–8	5–7	2150	Not reported.	[49]
Fe_2O_3	20–30	3.5	2000	0.50	[56]
Fe_2O_3	20	6.5	400	Not reported 1.7 mg/g at 32 µg/L	[57]
Iron oxide NPs	72	7	1000	less than 0.7 mg/g	[58]
Iron oxide NPs	7–11	3	8.4	Not reached	[23]
Ultra-small IONPs	1–3	5	30	3.5 ± 0.3	This work

which two contrary effects can explain: Fig. 3 shows that PVA-2 nanofibers have smaller IONPs than PVA-3 but more agglomerates distributed along the nanofibers.

Adsorption experiments were performed with the same dose of IONPs to evaluate the effect of IONPs' entrapment, so the mass of the membrane used was inversely proportional to the NP's content. This is a crucial consideration for escalation purposes, given that the polymer represents the highest membrane cost (80 % to 90 % according to materials cost in Argentina). It should be minimized to incorporate the membrane in a filtration system. In this sense, PVA-3 is the best option because it has three times more adsorbent than PVA-1, which is more than enough to compensate for the mean reduction in adsorption capacity of approximately 20 %.

Kinetics experiments were performed to enlighten the mechanism of arsenic interchange within the nanofibers, shown in Fig. 9(c). Adsorption kinetics of all the membranes followed the pseudo- second-order model (Eq. (6)), with a linear correlation coefficient higher than 0.989 for all the data. This suggests that chemisorption is the main adsorption mechanism [29,59]. Among the membranes, PVA-1 presented slightly faster adsorption, while PVA-2 and PVA-3 had similar and slower kinetics. This can be explained by the delay in species diffusion when more IONPs are present in the polymeric matrix. Pseudo-first order and Webber-Morris models were also tested, but they were less adequate to fit the data, as concluded by the reduced chi squared (χ^2_r) parameter and the plot fit residuals (fit plots and results shown in Fig. S7 and Table S2, respectively). The failure of Weber and Morris model is expected, as arsenic adsorption onto iron oxide nanoparticles is a surface phenomenon with no intraparticle diffusion mechanisms involved [60].

Moreover, the presence of agglomerates also delays the adsorption by making adsorption sites inaccessible. Nevertheless, the difference in adsorption velocity is much less significant than the differences in adsorption capacities, as depicted in isotherm studies. It is worth noting that kinetic experiments were performed at relatively low concentrations, where PVA-2 and PVA-3 adsorption isotherms do not differ significantly.

Fig. 9(d) shows that PVA-IONPs membranes can be reused after

arsenic adsorption, which is a key aspect towards escalation purposes. Moreover, adsorption capacity is higher than 80 % in the successive adsorption cycles of PVA-1 and PVA-2 membranes. Further studies showed that 8 h was sufficient time for desorption, provided that arsenic concentration of the regeneration solution reached equilibrium within the first 3 h.

The presence of phosphate anion in water is of particular interest because of its similar chemical structure to that of arsenate and its known interference with arsenic adsorption when using iron-based adsorbents [61]. We studied the effect of phosphate on arsenic uptake by the PVA-3 membrane at pH 4 and pH 5 (Fig. 10(a)). In both cases, phosphate reduces the removal efficiency from 84 % down to 43 %, which is a 51 % reduction in arsenic adsorption capacity. No significant difference can be observed when changing pH from 4 to 5, which can be explained by the prevalence of a single species of inorganic phosphate in solution (see inset of Fig. 10(b)). A similar reduction was observed in the literature for iron oxides such as magnetite [57,62]. At pH 5, the predominant phosphate species is $H_2PO_4^-$, similar to that of arsenate $H_2AsO_4^-$ found at the same pH. Given the high affinity of phosphate species to iron oxide nanoparticles, it competes with arsenic species for adsorption sites [61].

IONPs entrapped inside electrospun nanofibers can also be used to remove other water contaminants. Fig. 10(b) shows that the produced membranes can also adsorb Cr(VI) and Ni(II), with an 85 % removal efficiency of Cr(VI), which gives a chromium adsorption capacity of (8.0 ± 0.1) mg/g at 75 μg/L. This value dramatically exceeds those reported in the literature for removing Cr(VI) using iron oxides. For example, Kumari *et al.* achieved an adsorption capacity of less than 1.6 mg/g at 1000 μg/L and Chowdhury & Yanful less than 1 mg/g at 267 μg/L [63,64]. In our case, this adsorption is independent of the presence of Ni (II), suggesting the presence of heterogeneous adsorption sites, in accordance with the Freundlich model fitting As isotherms. The removal of Cr(VI) by iron oxides nanoparticles can be explained in terms of electrostatic attraction mechanism. It is well known that in the pH range 1–6 the main Cr(VI) species found in water is $HCrO_4^-$ while at pH > 6 the CrO_4^{2-} species is dominant [65]. Thus, it is expected that at pH 5 (pH at which the adsorption experiments were performed) the negatively charge $HCrO_4^-$ specie would be adsorbed onto the iron nanoparticles, which will be positively charged according to their pHpzc [48,49]. This result is consistent with the adsorption mechanism for chromium reported in the literature at pH < pHpzc [65], showing that it is possible to remove both metals without interference simultaneously.

Although less studied, non-iron-based As(V) adsorbents can be found in the literature, such as amine-based like chitosan [66], thiol-based like L-Cysteine [67], manganese oxides [68], among others [69]. Their adsorption capacity is strongly dependent on the initial (and equilibrium) concentrations. For example, Min *et al.* prepared a chitosan based electrospun nanofiber membrane, having an adsorption capacity of less than 12 mg/g for As(V) equilibrium concentration as high as 1000 μg/L [29]. Regarding other Cr(VI) adsorbents, several chitosan based materials have shown high adsorption capacities but usually testing on low pH (pH 3) and high equilibrium concentrations (above 20 mg/L) [70].

The efficiency of the membranes to retain the IONPs was evaluated. The iron content detected in the water for PVA-1 and PVA-2 membranes was (0.4 ± 0.1) mg/L and (0.3 ± 0.1) mg/L, respectively. These quantities represent (1.8 ± 0.4)% and (1.4 ± 0.5)% of the total iron content in each case. No significant differences were found, which indicates that for the same dose of IONPs used, iron leaching is independent of the mass fraction of IONPs in the membrane. Moreover, the developed PVA-1 and PVA-2 membranes were capable of retaining more than 98 % of the iron content during the simulated adsorption process.

4. Conclusions

We have shown a novel way to entrap iron oxide nanoparticles inside PVA nanofibers via an *in situ* approach. This strategy leads to a remarkable arsenic adsorption capacity of (3.5 ± 0.3) mg/g at a low As (V) concentration of 10 μg/L, significantly higher than those reported in the literature for loose adsorbents. Self-supporting, insoluble membranes could be effectively electrospun, containing up to 3 wt% of IONPs in a simple, straightforward, and green process. IONPs remain trapped in the nanofibers even after washing the membrane.

The presence and distribution of IONPs were confirmed using HR-TEM microscopy. DSC analysis showed that the presence of IONPs lowers the T_g of the polymer and alters its crystalline structure, suggesting that the IONPs distribute uniformly along the nanofibers. Adsorption isotherm studies showed that adsorption capacity is maximal at pH 5 and that the increase from 1 wt% to 3 wt% of IONPs content decreases the number of active sites for adsorption per unit mass of IONPs. Adsorption isotherms followed the Freundlich model, and kinetics followed the PSO model, both compatible with heterogeneous adsorption sites. The membranes obtained herein are reusable and have a high adsorption capacity for Cr(VI) independent of Ni(II) presence .

For the first time, it is shown the effect of increasing the NPs loading in the As adsorption capacity of a composite membrane, which serves as a mainstay for the development of nanoconfinement-mediated materials for water treatment.

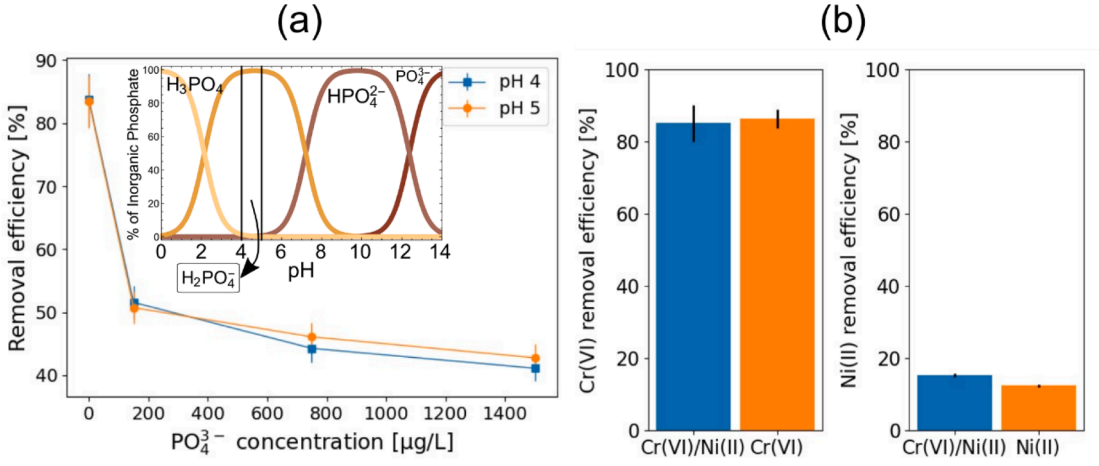

Fig. 10. (a) Removal efficiency of arsenic in the presence of phosphate ions at pH 4 and pH 5, with 600 μg/L initial arsenic concentration. Inset shows inorganic phosphate speciation. (b) Removal efficiency of Cr(VI) and Ni(II) starting from a solution containing only Cr(VI), Ni(II) or both (Cr(VI)/Ni(II)) at pH 5.

Declaration of Competing Interest

The authors declare that they have no known competing financial interests or personal relationships that could have appeared to influence the work reported in this paper.

Data availability

Data will be made available on request.

Acknowledgements

We kindly acknowledge the financial support of UBA (UBACYT 2018-2020 N°20020170100381BA), ANPCyT (PICT 2017-2362), MINCyT ("Programa Ciencia y Tecnología Contra el Hambre" IF-2021-4378615-APN-SSCI#MCT), CSIC (I-COOP2020 COOPB20502), the Ministerio de Ciencia, Innovación y Universidades code PID2019-104650 GB-C21 (MCIU/AEI/FEDER, UE) and IT1566-22 (Basque Government).

Appendix A. Supplementary data

Supplementary data to this article can be found online at https://doi.org/10.1016/j.cej.2022.140168.

References

[1] Transforming Our World: the 2030 Agenda for Sustainable Development A/RES/70/1 - United Nation general assembly, United Nations, 2015.
[2] M.I. Litter, A.M. Ingallinella, V. Olmos, M. Savio, G. Difeo, L. Botto, E.M. Farfán Torres, S. Taylor, S. Frangie, J. Herkovits, I. Schalamuk, M.J. González, E. Berardozzi, F.S. García Einschlag, P. Bhattacharya, A. Ahmad, Sci. Total Environ. 676 (2019) 756.
[3] H. Ritchie, M. Roser, Our World in Data, https://ourworldindata.org/clean-water-sanitation' **2021**.
[4] K. Noguera-Oviedo, D.S. Aga, J. Hazard. Mater. 316 (2016) 242.
[5] M. Patel, R. Kumar, K. Kishor, T. Mlsna, C.U. Pittman, D. Mohan, Chem. Rev. 119 (2019) 3510.
[6] WHO, Guidelines for drinking-water quality: fourth edition incorporating the first addendum. Geneva, 2017.
[7] E. Shaji, M. Santosh, K.V. Sarath, P. Prakash, V. Deepchand, B.V. Divya, Geosci. Front. 12 (2021), 101079.
[8] L. Weerasundara, Y.-S. Ok, J. Bundschuh, Environ. Pollut. 268 (2021), 115668.
[9] S. Bolisetty, M. Peydayesh, R. Mezzenga, Chem. Soc. Rev. 48 (2019) 463.
[10] Y. Bai, X. Tang, L. Sun, W. Yin, G. Hu, M. Liu, Y. Gong, Chem. Eng. J. 431 (2022), 134143.
[11] L. Hao, M. Liu, N. Wang, G. Li, RSC Adv. 8 (2018) 39545.
[12] S. Smita, S.K. Gupta, A. Bartonova, M. Dusinska, A.C. Gutleb, Q. Rahman, Environmental Health 11 (2012) S13.
[13] C. Egbuna, V.K. Parmar, J. Jeevanandam, S.M. Ezzat, K.C. Patrick-Iwuanyanwu, C. O. Adetunji, J. Khan, E.N. Onyeike, C.Z. Uche, M. Akram, M.S. Ibrahim, N.M. El Mahdy, C.G. Awuchi, K. Saravanan, H. Tijjani, U.E. Odoh, M. Messaoudi, J. C. Ifemeje, M.C. Olisah, N.J. Ezeofor, C.J. Chikwendu, C.G. Ibeabuchi, J. Toxicol. 2021 (2021) 9954443.
[14] G. Liu, C. Han, M. Kong, W.H.M. Abdelraheem, M.N. Nadagouda, D.D. Dionysiou, ACS ES&T Eng. 2 (2022) 1454.
[15] C.-H. Liu, Y.-H. Chuang, T.-Y. Chen, Y. Tian, H. Li, M.-K. Wang, W. Zhang, Environ. Sci. Technol. 49 (2015) 7726.
[16] A.A. Nayl, A.I. Abd-Elhamid, N.S. Awwad, M.A. Abdelgawad, J. Wu, X. Mo, S. M. Gomha, A.A. Aly, S. Bräse, Polymers 14 (2022) 1594.
[17] J. Cui, F. Li, Y. Wang, Q. Zhang, W. Ma, C. Huang, Sep. Purif. Technol. 250 (2020), 117116.
[18] S. Fahimirad, Z. Fahimirad, M. Sillanpää, Sci. Total Environ. 751 (2021), 141673.
[19] P. Bahmani, A. Maleki, H. Daraei, R. Rezaee, M. Khamforoush, S. Dehestani Athar, F. Gharibi, A.H. Ziaee, G. McKay, Environ. Sci. Pollut. Res. 26 (2019) 21993.
[20] P. Yadav, R. Farnood, V. Kumar, J. Environ. Chem. Eng. 9 (2021), 106507.
[21] E. Chiellini, A. Corti, S. D'Antone, R. Solaro, Prog. Polym. Sci. 28 (2003) 963.
[22] J. Cimadoro, S. Goyanes, J. Polym Sci. 58 (2020) 737.
[23] N. Torasso, A. Vergara-Rubio, P. Rivas-Rojas, C. Huck-Iriart, A. Larrañaga, A. Fernández-Cirelli, S. Cerveny, S. Goyanes, J. Environ. Chem. Eng. (2021), 104664.
[24] S. Wang, C. Wang, B. Zhang, Z. Sun, Z. Li, X. Jiang, X. Bai, Mater. Lett. 64 (2010) 9.
[25] R.T. Downs, M. Hall-Wallace, Am. Mineral. 88 (2003) 247.
[26] A. Jain, S.P. Ong, G. Hautier, W. Chen, W.D. Richards, S. Dacek, S. Cholia, D. Gunter, D. Skinner, G. Ceder, K.A. Persson, APL Mater. 1 (2013), 011002.
[27] J. Wang, X. Guo, Chemosphere 258 (2020), 127279.
[28] L. Yohai, H. Giraldo Mejía, R. Procaccini, S. Pellice, K. Laxman Kunjali, J. Dutta, A. Uheida, RSC Adv. 9 (2019) 8280.
[29] L.-L. Min, Z.-H. Yuan, L.-B. Zhong, Q. Liu, R.-X. Wu, Y.-M. Zheng, Chem. Eng. J. 267 (2015) 132.
[30] S.I. Siddiqui, S.A. Chaudhry, Process Saf. Environ. Prot. 111 (2017) 592.
[31] A. Vergara-Rubio, L. Ribba, D. Picón, R. Candal, S. Goyanes, Ind. Eng. Chem. Res. 61 (2022) 2091.
[32] D. Nataraj, R. Reddy, N. Reddy, Eur. Polym. J. 124 (2020), 109484.
[33] A. López-Córdoba, S. Estevez-Areco, S. Goyanes, Carbohydr. Polym. 215 (2019) 377.
[34] Y.H. Chen, J. Alloy. Compd. 553 (2013) 194.
[35] E.R. Monazam, R.W. Breault, R. Siriwardane, Ind. Eng. Chem. Res. 53 (2014) 13320.
[36] Y. Su, Y. Wu, M. Liu, Y. Qing, J. Zhou, Y. Wu, Materials 13 (2020) 1412.
[37] N. Mahanta, S. Valiyaveettil, RSC Adv. 3 (2013) 2776.
[38] F. Liu, Q.-Q. Ni, Y. Murakami, Text. Res. J. 83 (2013) 510.
[39] S. Mallakpour, M. Javadpour, Compos. Interfaces 22 (2015) 867.
[40] T.M. Kotresh, R. Ramani, N. Jana, S. Minu, R.I. Shekar, R. Ramachandran, ACS Appl. Polym. Mater. 3 (2021) 3989.
[41] Y.C. Jean, Microchem. J. 42 (1990) 72.
[42] N.J. Morales, R. Candal, L. Famá, S. Goyanes, G.H. Rubiolo, Carbohydr. Polym. 127 (2015) 291.
[43] T. Ahn, J.H. Kim, H.-M. Yang, J.W. Lee, J.-D. Kim, J. Phys. Chem. C 116 (2012) 6069.
[44] S. Kayal, R.V. Ramanujan, Mater. Sci. Eng., C 30 (2010) 484.
[45] J. Lee, T. Isobe, M. Senna, J. Colloid Interface Sci. 177 (1996) 490.
[46] R.A.B. John W., Bideaux, Kenneth W., Nichols, Monte C., eds, Handbook of Mineralogy. Vol. III (Halides, Hydroxides, Oxides). Mineralogical Society of America, Chantilly, VA, US, 1997.
[47] S. Goldberg, C.T. Johnston, J. Colloid Interface Sci. 234 (2001) 204.
[48] T. Tuutijärvi, J. Lu, M. Sillanpää, G. Chen, J. Hazard. Mater. 166 (2009) 1415.
[49] M. Kilianová, R. Prucek, J. Filip, J. Kolařík, L. Kvítek, A. Panáček, J. Tuček, R. Zbořil, Chemosphere 93 (2013) 2690.
[50] R. Kumar, M. Patel, P. Singh, J. Bundschuh, C.U. Pittman, L. Trakal, D. Mohan, Sci. Total Environ. 694 (2019), 133427.
[51] M. Shi, X. Min, Y. Ke, Z. Lin, Z. Yang, S. Wang, N. Peng, X. Yan, S. Luo, J. Wu, Y. Wei, Sci. Total Environ. 752 (2021), 141930.
[52] L.-L. Min, L.-B. Zhong, Y.-M. Zheng, Q. Liu, Z.-H. Yuan, L.-M. Yang, Sci. Rep. 6 (2016) 32480.
[53] M. Kanematsu, T.M. Young, K. Fukushi, P.G. Green, J.L. Darby, Environ. Sci. Technol. 44 (2010) 3388.
[54] M. Usman, I. Katsoyiannis, M. Mitrakas, A. Zouboulis, M. Ernst, Water 10 (2018) 957.
[55] S. Saif, A. Tahir, T. Asim, Y. Chen, S.F. Adil, Colloids and Interfaces 3 (2019) 17.
[56] V. Zaspalis, A. Pagana, S. Sklari, Desalination 217 (2007) 167.
[57] S.R. Chowdhury, E.K. Yanful, Water Environ. J. 25 (2011) 429.
[58] E. Di Iorio, C. Colombo, Z. Cheng, G. Capitani, D. Mele, G. Ventruti, R. Angelico, J. Environ. Chem. Eng. 7 (2019), 102986.
[59] B. Chen, Z. Zhu, S. Liu, J. Hong, J. Ma, Y. Qiu, J. Chen, ACS Appl. Mater. Interfaces 6 (2014) 14016.
[60] J. Wang, X. Guo, J. Hazard. Mater. 390 (2020), 122156.
[61] S. Dixit, J.G. Hering, Environ. Sci. Technol. 37 (2003) 4182.
[62] S. Luther, N. Borgfeld, J. Kim, J.G. Parsons, Microchem. J. 101 (2012) 30.
[63] M. Kumari, C.U. Pittman, D. Mohan, J. Colloid Interface Sci. 442 (2015) 120.
[64] S.R. Chowdhury, E.K. Yanful, J. Environ. Manage. 91 (2010) 2238.
[65] F. Yang, Y. Jiang, M. Dai, X. Hou, C. Peng, J. Hazard. Mater. 424 (2022), 127542.
[66] A.S.K. Kumar, S.-J. Jiang, J. Environ. Chem. Eng. 4 (2016) 1698.
[67] D. Picón, N. Torasso, J.R.V. Baudrit, S. Cerveny, S. Goyanes, Chem. Eng. Res. Des. 185 (2022) 108.
[68] S.M. Maliyekkal, L. Philip, T. Pradeep, Chem. Eng. J. 153 (2009) 101.
[69] J.P. Maity, C.-Y. Chen, P. Bhattacharya, R.K. Sharma, A. Ahmad, S. Patnaik, J. Bundschuh, J. Hazard. Mater. 405 (2021), 123885.
[70] M. Vakili, S. Deng, T. Li, W. Wang, W. Wang, G. Yu, Chem. Eng. J. 347 (2018) 782.